

Anharmonicity Driven by Vacancy Ordering Unlocks High-performance Thermoelectric Conversion in Defective Chalcopyrites II-III₂-VI₄

Hui Zhang^{1,†}, Jincheng Yue^{2,3,1,†,*}, Jiongzhi Zheng^{4,5}, Ning Wang¹, Wenling Ren⁶,
Shuyao Lin^{7,8}, Chen Shen^{9,10}, Hao Gao², Yanhui Liu^{1,*}, Yue-Wen Fang^{2,*}, Tian Cui^{1,*}

¹*Institute of High-Pressure Physics,*

School of Physical Science and Technology,

Ningbo University, Ningbo 315211, China

²*Centro de Física de Materiales (CFM-MPC),*

CSIC-UPV/EHU, Manuel de Lardizabal Pasealekua 5,

20018 Donostia/San Sebastián, Spain

³*Fisika Aplikatua Saila, Gipuzkoako Ingeniaritza Eskola,*

University of the Basque Country (UPV/EHU),

Europa Plaza 1, 20018 Donostia/San Sebastián, Spain

⁴*Energy Technologies Area, Lawrence Berkeley*

National Laboratory, Berkeley, CA 94720, USA

⁵*Thayer School of Engineering, Dartmouth College,*

Hanover, New Hampshire, 03755, USA

⁶*Institute of Materials Science, Technical University of Darmstadt,*

Alarich-Weiss-Strasse 2, Darmstadt, 64287, Germany

⁷*Technische Universität Wien, Institute of Materials*

Science and Technology, Vienna, A-1060, Austria

⁸*Linköping University, Department of Physics, Chemistry,*

and Biology (IFM), Linköping, SE-58183, Sweden

⁹*Suzhou Laboratory, Suzhou, China and*

¹⁰*Gusu Laboratory of Materials, Suzhou, China*

(Dated: March 18, 2026)

Abstract

Defective chalcopyrites have recently emerged as promising thermoelectric materials because their ordered intrinsic vacancies can profoundly reshape both lattice dynamics and electronic structure. Here, we present a comprehensive first-principles investigation of the thermal and carrier transport properties of II-III₂-VI₄ defective chalcopyrites. We show that vacancy ordering serves as a structural amplifier of lattice distortion, giving rise to strong lattice anharmonicity and metavalent-bonding character. In combination with soft low-frequency phonons, strongly negative Grüneisen parameters, and substantially enlarged four-phonon scattering phase space, this leads to four-phonon scattering-dominated heat transport and suppresses the lattice thermal conductivity to ultralow values. Meanwhile, systematic anion substitution at the VI-site provides an effective route to tune the electronic structure: decreasing anion electronegativity weakens metal-anion hybridization, shifts anion *p* states upward, narrows the band gap, and thereby improves electrical transport. Benefiting from this synergy between vacancy-induced phonon suppression and anion-regulated electronic optimization, CdGa₂Te₄ exhibits an ultralow lattice thermal conductivity of 0.19 W·m⁻¹K⁻¹ and a high room-temperature *ZT* of 0.957. These results establish a microscopic framework linking vacancy ordering, higher-order phonon scattering, and anion-dependent band engineering, and highlight defective chalcopyrites as a promising platform for high-performance thermoelectrics.

I. INTRODUCTION

Ternary diamond-like compounds have emerged as a research hotspot in the field of thermoelectric materials due to their unique crystal structures [1–4]. These materials inherit and extend the excellent structural characteristics of traditional binary semiconductors, among which representative systems with zinc-blende [5, 6], wurtzite [7, 8], and chalcopyrite [9–11] structures have been widely investigated. Chalcopyrite compounds (I-III-VI₂) are a well-known lattice-distorted thermoelectric material [12]. Their inherent lattice distortion induces strong lattice anharmonicity [13] and gives rise to ultralow lattice thermal conductivity (κ_L) that is a crucial foundation for high-performance thermoelectric materials [14]. It also exhibits high tunability of electronic band structures [15, 16]. For instance, substituting anionic components can effectively modulate the band gap, thereby optimizing electronic

transport properties [15]. To fully exploit the potential of these materials for applications, researchers have conducted extensive efforts in thermoelectric performance optimization in recent years. The main strategies include band engineering [17–19], element doping [20–22], and external control methods such as applying pressure [14, 16].

Although these external regulation methods can effectively improve thermoelectric performance, exploring compounds with intrinsic lattice distortion characteristics is crucial for fundamentally optimizing material properties [23, 24]. Xie et al. [25] recently demonstrated that the large tetrahedral distortion parameter η ($\eta = |2 - c/a|$) in silver-based chalcopyrites drives their intrinsic low lattice thermal conductivity. In-depth analysis reveals that this distortion induces strong lattice anharmonicity by breaking local tetrahedral symmetry, thereby significantly enhancing phonon scattering and ultimately suppressing the lattice thermal conductivity. Compared to traditional strategies that rely on external doping to introduce point defects for phonon scattering, intrinsic distortion achieves effective suppression of thermal transport through the inherent characteristics of the crystal structure, offering new possibilities for the development of a new generation of high-performance thermoelectric materials.

Defective chalcopyrites (II-III₂-VI₄) typically exhibit an ordered vacancy structure derived from the evolution of the chalcopyrite structure, achieved by doubling the original formula unit and removing one group-I atom, thereby creating vacancies at the original group-I atomic sites [25]. The chalcopyrite structure ($I\bar{4}2d$, No.122) itself can be traced back to the ternary diamondoid compounds, as shown in FIG. 1(a). It essentially comprises a double zincblende cell ($F\bar{4}3m$, No.216) stacked along the c -axis, where monovalent and trivalent cations replace the divalent cation. In zincblende, all tetrahedral coordination units exhibit perfect tetrahedral symmetry, characterized by cubic lattice parameters ($a = b = c$) and a unity tetragonal distortion ($\eta = 1$). While the tetrahedral framework is preserved, it results in a tetragonal distortion characterized by $\eta \neq 1$ and a deviation of bond angles from the ideal value (109.47°), collectively manifesting this initial breaking of tetrahedral symmetry. Further introduction of vacancies induces a second symmetry-lowering to $I\bar{4}$ (No. 82), thereby intensifying the lattice distortion. As a result, the symmetry is reduced from $F\bar{4}3m$ to $I\bar{4}2d$, and then further decreases to $I\bar{4}$. Low-symmetry thermoelectric materials typically feature low κ_L due to structure complexity. Therefore, defective chalcopyrites also exhibit ultralow lattice thermal conductivity, with a magnitude comparable to the low

κ_L reported in other thermoelectric materials [26–29]. This remarkable property renders it promising for thermoelectric applications, driving us to conduct systematic research on defective chalcopyrites.

In this work, we carry out a comprehensive investigation of the thermoelectric properties of defective chalcopyrites II-III₂-VI₄ by combining first-principles calculations with machine-learning interatomic potentials. We show that intrinsic vacancy ordering is not merely a crystallographic feature, but a key structural origin of the strong lattice anharmonicity in these materials. The vacancy-induced symmetry lowering and local lattice distortion promote metavalent-bonding character, soften low-frequency phonons, and enhance higher-order phonon interactions, ultimately rendering four-phonon scattering a dominant channel in suppressing lattice thermal conductivity. In parallel, we reveal a clear anion-dependent electronic trend: as the electronegativity of the VI-site anion decreases, weakened orbital hybridization and the upward shift of anion p states cooperatively narrow the band gap and improve electrical transport. As a result, CdGa₂Te₄ emerges as the best-performing member of this family, combining an ultralow lattice thermal conductivity of 0.19 W·m⁻¹K⁻¹ with a room-temperature ZT of 0.957. These findings clarify the coupled roles of vacancy ordering and anion engineering in regulating phonon and carrier transport, and provide a viable design strategy for high-performance chalcopyrite-based thermoelectric materials.

II. COMPUTATIONAL METHODS

A. Density functional theory calculations

The Vienna Ab initio Simulation Package (VASP) [30, 31] was used to perform first-principles density functional theory (DFT) calculations. The Perdew-Burke-Ernzerhof revised for solids (PBEsol) functional [32] within the generalized gradient approximation (GGA) [33] was applied to describe the exchange-correlation effects. The projector augmented wave (PAW) [34] method was used to treat the Cd($4d^{10}5s^2$), Zn($3d^{10}4s^2$), In($4d^{10}5s^25p^1$), Ga($3d^{10}4s^24p^1$), S($3s^23p^4$), Se($4s^24p^4$) and Te($5s^25p^4$) shells as valence states. The energy and force convergence standards for structural optimization were 10^{-8} eV and 10^{-4} eV·Å⁻¹, respectively. A kinetic energy cutoff of 500 eV and a $16 \times 16 \times 8$ Monkhorst-Pack k -point grid were adopted to sample the Brillouin zone for the primitive cell.

B. Machine-learning interatomic potentials

1. Moment tensor potential.

The moment tensor potentials (MTPs) [35, 36], which have been well validated in reproducing DFT-level results [37, 38], was used to evaluate the interatomic forces. The training of MTPs is done by solving the following minimization problem:

$$\sum_{k=1}^K \left[w_e (E_k^{DFT} - E_k^{MTP})^2 + w_f \sum_i^N |f_{k,i}^{DFT} - f_{k,i}^{MTP}|^2 + w_s \sum_{i,j=1}^3 |\sigma_{k,ij}^{DFT} - \sigma_{k,ij}^{MTP}|^2 \right] \rightarrow \min, \quad (1)$$

where E_k^{DFT} , $f_{k,i}^{DFT}$, and $\sigma_{k,ij}^{DFT}$ are the energy, atomic forces, and stresses in the training set, respectively, and E_k^{MTP} , $f_{k,i}^{MTP}$, and $\sigma_{k,ij}^{MTP}$ are the corresponding values calculated with the MTP. K is the number of configurations in the training set, N is the number of atoms in a configuration. The variables w_e , w_f , and w_s are the non-negative weights that express the importance of energies, forces, and stresses in the optimization problem, which in our study were set to 1, 0.1, and 0.001, respectively. The training sets were generated using ab initio molecular dynamics (AIMD). We performed simulations using $3 \times 3 \times 3$ supercells containing 189 atoms in the canonical (NVT) ensemble at temperatures of 20, 50, 100, 200, and 300 K.

During the simulations, one configuration was sampled every 5 time steps for a total of 3000 time steps. For each configuration, we further employed a tight energy convergence criterion of 10^{-8} eV to perform DFT calculations with a $3 \times 3 \times 3$ Monkhorst-Pack k -mesh. The MTP-predicted results closely match the DFT calculations, yielding maximum root-mean-square errors (RMSE) of $0.063 \text{ meV} \cdot \text{atom}^{-1}$ for energies and $0.029 \text{ eV} \cdot \text{\AA}^{-1}$ for forces, respectively. Comparisons between DFT calculations and model predictions are shown in FIGs. S1 and S2 in the Supporting Information.

2. Deep potential

The deep potential (DP) model, as implemented in the DeepMD-kit package [39], was constructed and trained using the same training data as above MTP. In the DP model, the total energy E is a sum of atomic energies E_i , each predicted by an embedding network from a local descriptor D_i that encodes the environment of atom i within a cutoff of 8 \AA while preserving translational, rotational and permutational symmetry. To eliminate the spurious discontinuities introduced by the sharp cutoff, the smooth-edition DP potential [40] was adopted. The embedding network expands radial information through three hidden layers of 25, 50 and 100 neurons, while the fitting network (3×240 neurons) is wired as a residual net to accelerate convergence. The loss function is defined as

$$L(p_\epsilon, p_f, p_\xi) = p_\epsilon \Delta\epsilon^2 + \frac{p_f}{3N} \sum_i |\Delta F_i|^2 + \frac{p_\xi}{9} \|\Delta\xi\|^2 \quad (2)$$

where $\Delta\epsilon$, ΔF_i , and $\Delta\xi$ represent the energy, force, and virial tensor difference between the DP model prediction and the training dataset. The p_ϵ , p_f , and p_ξ are weight coefficients of energy, force, and virial tensor. The p_ϵ is set to increase from 0.02 to 1, while the p_f is decreased from 1000 to 1 during the training procedure. The DP models are trained with 1,000,000 steps. The results indicate a good agreement between DP predictions and DFT calculations with RMSE less than $0.26 \text{ meV} \cdot \text{atom}^{-1}$ and $0.019 \text{ eV} \cdot \text{\AA}^{-1}$ for energies and forces, respectively. Comparisons are shown in FIGs. S3 and S4 in the Supporting Information. In addition, we performed MD simulations of the NVT using the DP model with a time step of 10 fs and a total simulation time of 100 ps, as implemented in the FHI-vibes package [41]. The corresponding potential energy and thermostat dynamics are shown in FIG. S5 of the Supporting Information.

C. Lattice thermal conductivity calculation

For harmonic interatomic force constants (IFCs), we used the finite displacement method [42] where an atom in the supercell ($3\times 3\times 3$) was displaced from its equilibrium site by 0.01 Å, as implemented in the Phonopy package [43, 44]. The Hellmann-Feynman forces were calculated for the displaced configuration by DFT with an energy convergence criterion of 10^{-8} eV and $3\times 3\times 3$ Monkhorst-Pack k -mesh. Third- and fourth-order IFCs were obtained analogously, with interactions extended up to the 18th and 5th nearest-neighbor shells, respectively, using the Thirdorder [45] and Fourthorder [46] packages. It is worth noting that approximately 3,000 and 25,000 displacement configurations were generated under this setting, respectively. Therefore, we used the previously generated MTP-based MLIPs to obtain the energies and forces for all generated configurations. To verify the reliability of the energy and force constants obtained by MTP-based MLIPs for displacement configurations, we randomly selected 300 structures and performed DFT calculations for comparison. The results show that the RMSE of the forces for all compounds is less than $0.002 \text{ eV}\cdot\text{Å}^{-1}$, as shown in FIG. S6 of the Supporting Information.

Within the linearized Wigner transport equation (LWTE) framework [47], the κ_L using the two-channel model can be described as [47]:

$$\kappa_L = \frac{1}{N_q V} \sum_{qqj'} \frac{c_{qj}\omega_{qj'} + c_{qj'}\omega_{qj}}{\omega_{qj} + \omega_{qj'}} v_{qjj'} \otimes v_{qj'j} \times \frac{\Gamma_{qj} + \Gamma_{qj'}}{(\omega_{qj} - \omega_{qj'})^2 + (\Gamma_{qj} + \Gamma_{qj'})^2} \quad (3)$$

where the c_{qj} , V , and N_0 are the mode heat capacity, primitive-cell volume, and number of samples, respectively. The $v_{qjj'} = 1/2(\omega_{qj}\omega_{qj'})^{-1/2} \langle \eta_{qj'} | \partial_q C(q) | \eta_{qj} \rangle$ represents the generalized interband group velocity with $C(q)$ and η_{qj} being the dynamical matrix and polarization vector, respectively. The band diagonal term ($j = j'$) corresponds to the Peierls contribution (κ_P) within the relaxation-time approximation [48], while the off-diagonal term gives the coherent contribution (κ_C); the total lattice thermal conductivity is given as $\kappa_L = \kappa_P + \kappa_C$. The Γ_q stands for the scattering rates including three-phonon ($3ph$), four-phonon ($4ph$), and isotope-phonon scattering processes. In this work, the q mesh for phonon scattering processes was set to $16 \times 16 \times 16$. And we used an adaptive Gaussian smearing with a smearing scale of 0.1 for the calculation of phonon lifetimes, which gives well-converged results. The convergence results are presented in FIG. S7 in the Supporting Information.

D. Electrical transport calculation

The related electronic-structure and transport calculations were carried out using the Heyd-Scuseria-Ernzerhof (HSE) [49] adjusted band gap, employing the VASP and AMSET [50] codes, respectively. We simulated the effects of three major scattering mechanisms: acoustic deformation potential scattering (ADP), polar optical phonon scattering (POP), and ionized impurity scattering (IMP) on the electronic transport properties during the carrier transport process [50, 51]. The transition rates of electrons from the initial $\psi_{n\mathbf{k}}$ to final states $\psi_{m\mathbf{k}+\mathbf{q}}$ were based on Fermi's golden rule [52], which can be expressed as

$$\tilde{\tau}_{n\mathbf{k} \rightarrow m\mathbf{k}+\mathbf{q}}^{-1} = \frac{2\pi}{\hbar} |g_{nm}(\mathbf{k}, \mathbf{q})|^2 \delta(\varepsilon_{n\mathbf{k}} - \varepsilon_{m\mathbf{k}+\mathbf{q}}) \quad (4)$$

where $\varepsilon_{n\mathbf{k}}$ symbolizes the specific energy state $\psi_{n\mathbf{k}}$. The $g_{nm}(\mathbf{k}, \mathbf{q})$ accounts for three kinds of electron-phonon scattering matrix elements. The relaxation time of each electron can be evaluated by Matthiessen's rule [53], which is followed by

$$\tau_{n\mathbf{k}}^{-1} = \tau_{\text{ADP}}^{-1} + \tau_{\text{POP}}^{-1} + \tau_{\text{IMP}}^{-1} \quad (5)$$

The transport tensors can be calculated from the conductivity distributions

$$\sigma_{\alpha\beta}(T, \mu) = \frac{1}{\Omega} \int \sigma_{\alpha\beta}(\varepsilon) \left[-\frac{\partial f_{\mu}(T; \varepsilon)}{\partial \varepsilon} \right] d\varepsilon \quad (6)$$

$$\nu_{\alpha\beta}(T; \mu) = \frac{1}{eT\Omega} \int \sigma_{\alpha\beta}(\varepsilon)(\varepsilon - \mu) \left[-\frac{\partial f_{\mu}(T; \varepsilon)}{\partial \varepsilon} \right] d\varepsilon \quad (7)$$

$$S_{ij} = E_i(\nabla_j T)^{-1} = (\sigma^{-1})_{\alpha i} v_{\alpha j} \quad (8)$$

$$\kappa_{\alpha\beta}^0(T; \mu) = \frac{1}{e^2 T \Omega} \int \sigma_{\alpha\beta}(\varepsilon)(\varepsilon - \mu)^2 \left[-\frac{\partial f_{\mu}(T; \varepsilon)}{\partial \varepsilon} \right] d\varepsilon \quad (9)$$

where $\sigma_{\alpha\beta}$, $\sigma_{\alpha\beta}(\varepsilon)$, Ω , $f_{\mu}(T; \varepsilon)$, e , ε and κ^0 represent the conductivity tensor, conductivity distribution function, cell volume, Fermi-Dirac distribution function, charge, energy and electronic part of the thermal conductivity.

III. RESULTS AND DISCUSSION

The potentially ultralow κ_L arising from vacancy-driven symmetry breaking motivates our systematic investigation of defective chalcopyrites. Before exploring their thermoelectric performance, we first verify their mechanical stability, which is a prerequisite for practical applications through elastic constant calculations. As summarized in Table S1, all compounds satisfy the Born stability criteria [54], confirming their mechanical stability and paving the way for subsequent transport analysis. The calculated elastic constants for all compounds satisfy these criteria, thereby confirming their intrinsic mechanical stability under ambient conditions. It is worth noting that the elastic moduli show a consistent decrease as the electronegativity of the VI-site anion decreases with the cation fixed, which reflects the weakening of the average bond strength due to the increase in anion mass. Additionally, the convex hull diagrams related to the thermodynamics of all compounds were obtained from the Open Quantum Materials Database (OQMD) [55, 56] and are provided in FIG. S8 of the Supporting Information. Convex hull analysis reveals that most compounds exhibit thermodynamic stability, as they reside on the convex hull ($0 \text{ meV}\cdot\text{atom}^{-1}$). In contrast, CdIn_2S_4 and ZnIn_2S_4 are located above the hull (greater than $0 \text{ meV}\cdot\text{atom}^{-1}$) and are therefore metastable phases. Although ZnIn_2S_4 lies above the convex hull, it has been reported to be successfully synthesized [57], suggesting that metastable phases can still be realized under appropriate experimental conditions.

Based on the combined mechanical and thermodynamic stability analyses, we investigated the thermoelectric performance of defective chalcopyrites. As mentioned, the distortion parameter η not only critically influences κ_L but also serves as a fundamental indicator of lattice anharmonicity. Generally, one larger η indicates the greater deviation of the chalcopyrite lattice from the ideal diamond structure [15]. Such a structural distortion directly reflects an increase in lattice anharmonicity, which in turn effectively suppresses lattice thermal conductivity. As shown in FIG. 1(b), the ZnSe, with an ideal cubic zinc-blende structure ($\eta = 0$), shows a relatively high κ_L . As the lattice undergoes tetragonal distortion to chalcopyrite, the κ_L significantly decreases. This trend clearly demonstrates that κ_L is strongly suppressed as η increases because of the enhanced lattice anharmonicity. Moreover, defective chalcopyrites possess lower-symmetry space groups and exhibit more strongly distorted frameworks than chalcopyrite due to the presence of intrinsic cation vacancies. As

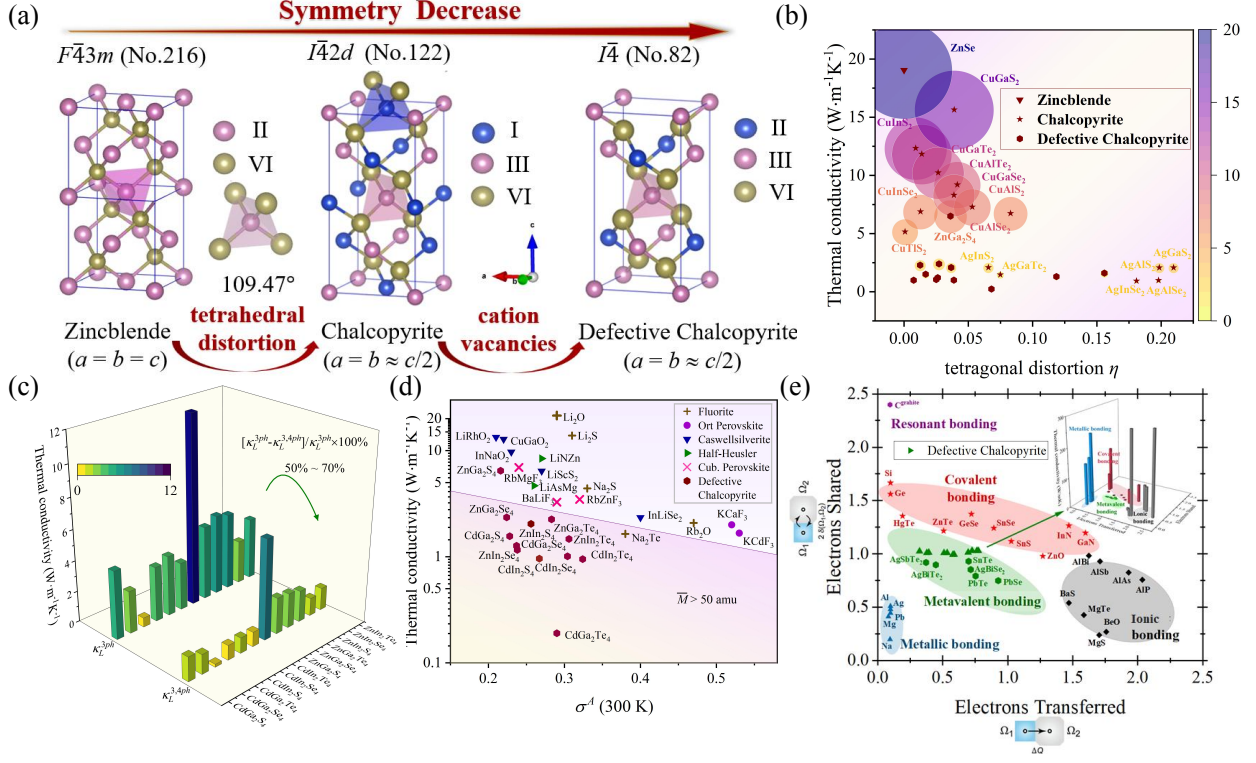


FIG. 1. (a) The crystal structure of zincblende ($F\bar{4}3m$, No.216), chalcopyrite ($I\bar{4}2d$, No.122), and defective chalcopyrites ($I\bar{4}$, No.82). The tetrahedra represent the coordination environments. The ideal bond angle of a perfect tetrahedron ($a = b = c$) is 109.47° . The arrow represents a decrease in the space group. The blue and pink represent cations, while the yellow denotes anions. (b) The relationship between the η and the κ_L of different compounds. The related zincblende and chalcopyrite data are available in ref. [25]. (c) The κ_L evaluated by including both $3ph$ and $4ph$ scattering processes ($\kappa_L^{3,4ph}$) and by accounting for only $3ph$ scattering processes (κ_L^{3ph}). The color scale represents the κ_L . To calculate the relative reduction in the κ_L , subtract $\kappa_L^{3,4ph}$ from κ_L^{3ph} , then divide by the latter and multiply by 100%. (d) The κ_L as a function of the lattice anharmonicity measure σ^A at 300 K. The red hexagon represents defective chalcopyrites, with data for other compounds given in ref. [58]. With the purple line in the figure as the boundary, the materials in the upper region have a $\bar{M} < 50$ amu, while those in the lower region have a $\bar{M} > 50$ amu. (e) The quantum mechanics diagram of bonding in solids, with coordinates representing the number of electrons shared and transferred between adjacent atoms. The green triangle represents defective chalcopyrites, and data for other compounds can be found in ref. [59].

expected, defective chalcopyrites are characterized by intrinsically low thermal conductivity, underscoring their potential as promising thermoelectric materials.

Chalcopyrites inherently exhibit pronounced phonon scattering driven by tetrahedral distortion, making higher-order processes indispensable for an accurate description [12, 14, 60]. Indeed, in CuInTe₂, the incorporation of $4ph$ scattering results in a substantial reduction of κ_L by 54.6% at 800 K [61]. By contrast, defective chalcopyrites experience even stronger anharmonic scattering, arising from the cooperative effects of tetrahedral distortion and vacancy-induced local lattice perturbations. FIG. 1(c) shows the κ_L (including $3ph$ and $4ph$ scattering) as a function of temperature for defective chalcopyrites. Our results reveal that the inclusion of $4ph$ scattering leads to a 50–70% reduction in thermal conductivity in defective chalcopyrites at 300 K. Specifically, for CdGa₂Te₄, the inclusion of $4ph$ scattering at 300 K reduces κ_L from 0.61 W·m⁻¹K⁻¹ (with only $3ph$ scattering) to 0.19 W·m⁻¹K⁻¹, corresponding to a reduction of 68%. In addition, when only $3ph$ scattering is considered, the calculated κ_L of ZnIn₂Te₄ and CdIn₂Te₄ are 4.05 W·m⁻¹K⁻¹ and 3.12 W·m⁻¹K⁻¹ at 300 K, respectively. These values are substantially higher than the experimentally reported κ_L of 2.1 W·m⁻¹K⁻¹ for ZnIn₂Te₄ and 1.2 W·m⁻¹K⁻¹ for CdIn₂Te₄ [26], indicating that a description based solely on third-order anharmonicity overestimates κ_L . Upon explicitly incorporating $4ph$ scattering processes, the predicted κ_L are significantly reduced to 1.47 W·m⁻¹K⁻¹ and 0.95 W·m⁻¹K⁻¹ for ZnIn₂Te₄ and CdIn₂Te₄, respectively, yielding much closer agreement with experiment. These results suggest that the cooperative effects of tetrahedral distortion and cation vacancies give rise to strong $4ph$ scattering processes, whose contributions are essential for a reliable quantitative evaluation of κ_L in defective chalcopyrites.

To quantify the strength of anharmonic effects in a material, we calculate the anharmonicity index $\sigma^A(T)$, defined as [62]:

$$\sigma^A(T) \equiv \frac{\sigma [F^A]_T}{\sigma [F]_T} = \sqrt{\frac{\sum_{I,\alpha} \langle (F_{I,\alpha}^A)^2 \rangle_T}{\sum_{I,\alpha} \langle (F_{I,\alpha})^2 \rangle_T}} \quad (10)$$

Here, $F_{I,\alpha}(t) \equiv F_{I,\alpha}[\mathbf{R}(t)]$ denotes the α component of the force acting on atom I at time t , and $F_{I,\alpha}^A$ is the anharmonic contribution to that force component. A value of $\sigma^A(T) > 0.2$ indicates that anharmonic interactions become comparable in magnitude to harmonic interactions [62]. As shown in FIG. 1(d), $\sigma^A(T = 300 \text{ K})$ for defective chalcopyrites primarily lies in the range of 0.22–0.33. Among them, ZnGa₂S₄ exhibits the smallest $\sigma^A(300 \text{ K})$

and the largest κ_L ($6.46 \text{ W}\cdot\text{m}^{-1}\text{K}^{-1}$), whereas CdIn_2Te_4 shows the largest $\sigma^A(300 \text{ K})$ and a much lower κ_L ($0.95 \text{ W}\cdot\text{m}^{-1}\text{K}^{-1}$). Extending the analysis to a broader range of materials with $\sigma^A(300 \text{ K})$ values from 0.2 to 0.6, including simple binary compounds, perovskites, and chalcopyrite-type systems, most materials are found to possess κ_L below $10 \text{ W}\cdot\text{m}^{-1}\text{K}^{-1}$. Notably, defective chalcopyrites tend to exhibit even lower κ_L than other materials at comparable levels of anharmonicity. This behavior can be largely attributed to their relatively high mean atomic mass (\bar{M}) and the presence of intrinsic vacancies. Most of the defective chalcopyrites have an \bar{M} greater than 50 amu (except ZnGa_2S_4 at 47.58 amu) [63]. This is noteworthy because materials with higher κ_L typically consist of lighter atoms. Except for ZnGa_2S_4 ($\bar{M}= 47.58$ amu), most defective chalcopyrites have \bar{M} values exceeding 50 amu, whereas materials with higher κ_L typically possess lighter constituent atoms. These results suggest that the ultralow κ_L in defective chalcopyrites arises from the synergistic effects of strong lattice anharmonicity, heavy atomic masses, and vacancy-induced phonon scattering.

On the other hand, intrinsic low thermal conductivity is closely linked to the nature of its atomic bonding. FIG. 1(e) summarizes the charge transfer and the number of shared electron pairs based on atomic net charge Q_i (reflecting electron transfer) and delocalization index $\delta(\Omega_i, \Omega_j)$ (quantifying covalent interactions between atoms). These two descriptors clearly delineate bonding regimes associated with ionic, covalent, metallic, and metavalent (MVB) bonding. Notably, defective chalcopyrites lie within the central green region, which corresponds to the MVB domain characterized by distinct transitional bonding behavior. Its bonding is marked by approximately 0.8 shared electrons per bond—intermediate between conventional covalent bonding with highly localized electron sharing and metallic bonding with strongly delocalized electrons. Such unconventional bonding is considered the origin of its exceptionally low lattice thermal conductivity [64–66], as highlighted in the inset of FIG. 1(e). Microscopically, this behavior arises from strong bond-induced lattice anharmonicity, manifested as a large Grüneisen parameter [59]. Previous studies have shown that the intrinsically distorted tetrahedral configuration in silver-based chalcopyrite materials AgXY_2 promotes the formation of MVB bonding [67], leading to the softening of low-frequency optical phonons and the suppression of κ_L . As a result, cation vacancies in defective chalcopyrites induce lattice distortion that promotes MVB formation and thereby introduces strong lattice anharmonicity which ultimately leads to its extremely low lattice thermal conductivity.

For a comprehensive investigation of thermal transport behaviors, CdGa_2Te_4 and ZnGa_2S_4 with the lowest and highest κ_L were selected for comparison. As shown in FIG. 2(a), the calculated phonon dispersions of CdGa_2Te_4 and ZnGa_2S_4 exhibit no imaginary modes, confirming their dynamical stability. The two compounds nevertheless differ markedly in the low-frequency region. The ZnGa_2S_4 possesses a higher-lying lowest acoustic branch across the Brillouin zone, whereas softer acoustic phonons characterize CdGa_2Te_4 . To quantify the long-wavelength lattice vibrations, we linearly fitted the lowest acoustic branch along the Γ –M direction. The fitted slope for ZnGa_2S_4 is 2.04, which is substantially larger than the value of 0.61 obtained for CdGa_2Te_4 , implying a higher acoustic phonon group velocity in ZnGa_2S_4 . This trend is mainly associated with the larger average atomic mass of CdGa_2Te_4 , which lowers vibrational frequencies and is expected to suppress lattice thermal conductivity.

Consistent with FIG. 2(a), the phonon density of states (DOS) in FIG. 2(b) shows that CdGa_2Te_4 is characterized by pronounced peaks dominated by Cd- and Te-derived vibrations, reflecting the dominant role of heavy atoms in low-frequency modes. In contrast, ZnGa_2S_4 displays broader DOS features arising from the collective contributions of Zn, Ga, and S. Furthermore, we plotted the Grüneisen parameter for CdGa_2Te_4 and ZnGa_2S_4 in FIG. 2(c). Within the 0–2 THz range, the Grüneisen parameter of ZnGa_2S_4 stays close to zero and only reaches a mildly negative value of about -1.6 , showing no pronounced peak and thus indicating relatively weak anharmonicity. Conversely, CdGa_2Te_4 exhibits a strongly negative Grüneisen parameter over the same frequency window, with a pronounced minimum of around -10 . This large negative value suggests that the presence of heavy atoms is closely linked to strong lattice anharmonicity, which in turn promotes enhanced higher-order phonon–phonon scattering.

FIG. 2(d) evaluates how third- and fourth-order anharmonicity influences the phonon lifetime $\tau_{3,4ph}$ at 300 K. CdGa_2Te_4 exhibits markedly shorter $\tau_{3,4ph}$ than ZnGa_2S_4 , and the gap in the low-frequency region exceeds one order of magnitude. Such a difference is not caused by a single factor; rather, it reflects the combined roles of phonon group velocity and lattice anharmonicity. Specifically, the reduced group velocity in CdGa_2Te_4 indicates slower phonon propagation and therefore less efficient heat transport. At the same time, within the frequency interval where the Grüneisen parameter shows pronounced negative peaks, the low-frequency modes that are mainly associated with the heavy Cd and Te atoms experience

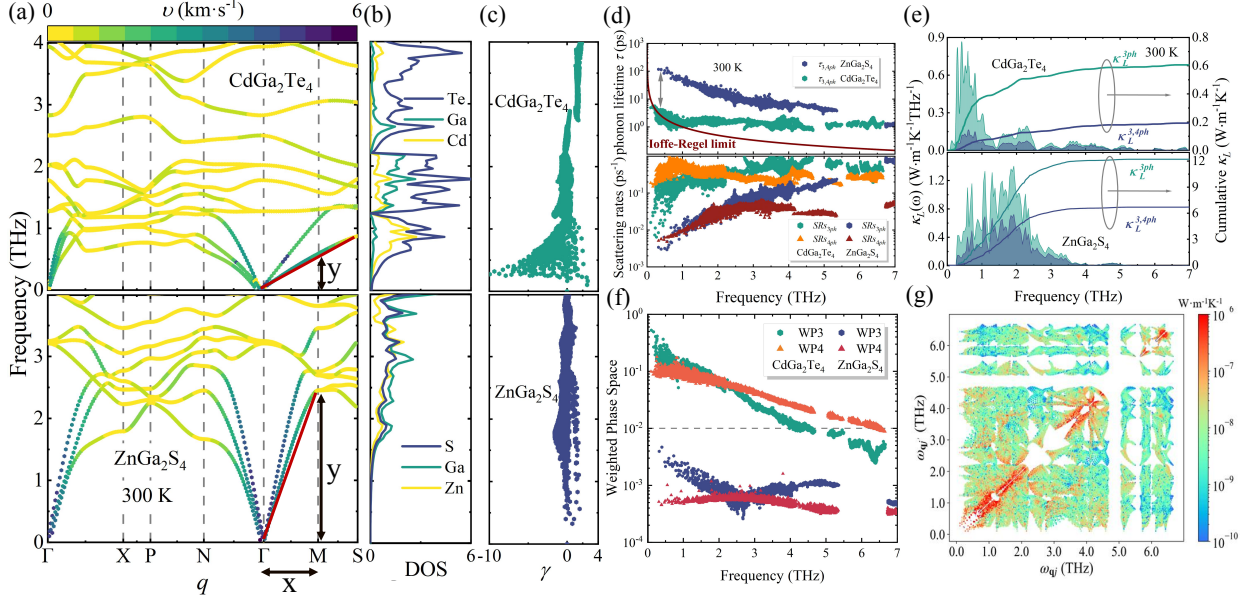


FIG. 2. Calculation of the thermal transport properties of CdGa₂Te₄ and ZnGa₂S₄. (a) Phonon dispersion relations at 300 K in the 0–4 THz frequency range. Along the Γ –M direction, the red line represents the linear fit to the acoustic branch, with its slope corresponding to the phonon group velocity. (b) The phonon density of states. In CdGa₂Te₄, the yellow, blue, and green curves represent the contributions of Cd, Te, and Ga atoms, respectively. In ZnGa₂S₄, the yellow, blue, and green curves represent the contributions of Zn, S, and Ga atoms, respectively. (c) The Grüneisen parameters γ . Green corresponds to CdGa₂Te₄, and blue corresponds to ZnGa₂S₄. (d) Phonon lifetimes $\tau_{3,4ph}$ including $3ph$ and $4ph$ scattering processes, as well as the $3ph$ (SRs_{3ph}) and $4ph$ (SRs_{4ph}) scattering rates of ZnGa₂S₄ and CdGa₂Te₄. Green and orange denote CdGa₂Te₄, blue and red denote ZnGa₂S₄. The red solid line indicates the Ioffe-Regel limit. (e) The spectral/cumulative thermal conductivity. κ_L^{3ph} represents only $3ph$ processes. $\kappa_L^{3,4ph}$ represents both $3ph$ and $4ph$ processes. The direction of the arrow points to the cumulative thermal conductivity. (f) Three- and four-phonon weighted phase space. Hexagons denote WP3 and triangles denote WP4; orange and green symbols correspond to CdGa₂Te₄, whereas red and azure blue symbols correspond to ZnGa₂S₄. (g) The calculated $\kappa_C(\omega_{qj}, \omega_{qj'})$ for CdGa₂Te₄ at 300 K. The diagonal data points ($\omega_{qj} = \omega_{qj'}$) indicate phonon degenerate eigenstates.

stronger anharmonic interactions, which further shorten the phonon lifetime. In addition, CdGa₂Te₄ exhibits a $4ph$ scattering rate in the low-frequency range that is roughly an order of magnitude higher than the $3ph$ scattering rate, demonstrating that $4ph$ processes

dominate the scattering and significantly suppress the $\tau_{3,4ph}$. By comparison, ZnGa_2S_4 shows similar magnitudes of $3ph$ and $4ph$ scattering rates in the same low-frequency region, implying comparable contributions from the two channels. When the frequency increases beyond 3.5 THz, $3ph$ scattering becomes the main scattering mechanism in both materials; this trend is particularly evident in ZnGa_2S_4 , where the $3ph$ rate clearly exceeds the $4ph$ rate. Taken together, the sharp reduction of phonon lifetime in CdGa_2Te_4 can be mainly attributed to the strongly enhanced higher-order scattering. In combination with its lower phonon group velocity, this leads to a stronger suppression of thermal transport in CdGa_2Te_4 than in ZnGa_2S_4 .

FIG. 2(e) presents the spectral and cumulative κ_L after including $4ph$ scattering. For CdGa_2Te_4 , the reduction of κ_L caused by $4ph$ scattering is mainly located in 0–1.5 THz. The spectral heat-carrying contributions associated with $4ph$ and $3ph$ scattering show little overlap in this interval, which indicates that low-frequency heat transport is largely controlled by $4ph$ scattering. By contrast, although $4ph$ scattering in ZnGa_2S_4 also decreases κ_L to some extent especially in 1–3 THz, its overall impact is weaker than in CdGa_2Te_4 . Further insight into this contrast is obtained from the weighted phase space in FIG. 2(f). The $4ph$ weighted phase space (WP4) of CdGa_2Te_4 is about two orders of magnitude larger than that of ZnGa_2S_4 , which points to a larger number of available $4ph$ scattering channels. Remarkably, WP4 is comparable to the $3ph$ weighted phase space (WP3) in CdGa_2Te_4 , so that $4ph$ and $3ph$ scattering share similar phase-space and higher-order processes can occur with high probability [46]. In ZnGa_2S_4 , however, WP3 remains dominant in 0–2 THz. Only in 2–3 THz does WP4 become comparable to WP3, a trend that is consistent with the phonon spectrum of ZnGa_2S_4 . Hence, in CdGa_2Te_4 the substantial WP4 and the pronounced intrinsic anharmonicity work together, where the former provides scattering channels, and the latter strengthens phonon–phonon coupling. Together, they markedly enhance the scattering rate, thereby severely suppressing the lattice thermal conductivity.

To examine whether the $4ph$ scattering necessarily involves a wave-tunneling phonon transport channel [68, 69], we calculated the coherent lattice thermal conductivity of CdGa_2Te_4 , as shown in FIG. 2(g) and FIG. S9. The results indicate that quasi-degenerate phonon modes ($\omega_{qj} \approx \omega_{qj'}$) provide the main contribution to the coherent conductivity [47]. The maximum value of this contribution is only $10^{-6} \text{ W}\cdot\text{m}^{-1}\text{K}^{-1}$, negligible compared with the total lattice thermal conductivity. Thus, while the $4ph$ scattering process serves as a key

mechanism for suppressing κ_L in defective chalcopyrites, the associated coherent phonon transport channel contributes only marginally to heat conduction and can be neglected.

As shown in FIG. 3(a), there is a strong correlation between bond length, tetragonal distortion, and the band gap E_g in defective chalcopyrites. For the CdGa_2X_4 ($\text{X} = \text{S}, \text{Se}, \text{Te}$), both Cd–X and Ga–X bond lengths increase monotonically as the electronegativity of the VI-site anion decreases with the cation fixed, accompanied by an increase in η from 0.922 to 0.996, approaching the cubic limit of $\eta = 1$. In parallel, the calculated E_g decreases markedly with increasing bond length, and the same monotonic trend is also observed in the Zn-based counterparts. Since PBE tends to underestimate E_g , HSE results are included to provide a consistent comparison of the gap evolution. The above trend originates from the differences in the intrinsic properties of the anions. As the electronegativity of the VI-site anion decreases with the cation fixed, the atomic radius increases [70]. This weakens the cation-anion bonding, directly leading to an increase in bond lengths. Meanwhile, the tetragonal distortion gradually diminishes, and the lattice symmetry approaches that of the cubic phase. These two factors collectively influence the electronic band structure, resulting in a monotonic decrease in the E_g with increasing anion atomic number.

To understand the microscopic origin of the gap reduction, the band structure, atom-projected DOS, and bonding analysis for CdGa_2Te_4 are calculated and shown in FIGs. 3(b)–(e). The band structure indicates a direct gap at Γ , with pronounced band degeneracy at the valence band maximum (VBM). As the electronegativity of the VI-site anion decreases with the cation fixed, the band degeneracy at the VBM gradually decreases, while the band curvature near the Fermi level increases correspondingly (see Supplementary FIGs. S10–S12 for details). This increased curvature results in relatively flat band regions, which correspond to a large density of states and a heavier carrier effective mass. The projected DOS shows that the VBM is dominated by Te-5*p* states, while the conduction band minimum (CBM) mainly originates from Ga-*s* states with appreciable Te-*p* admixture. Cd-*d* states are largely localized at deeper energies, yet their hybridization with anion *p* states can contribute to the *p*–*d* repulsion that shapes the valence edge. The bonding schematic in FIG. 3(d) provides an intuitive explanation for the aforementioned electronic structure features from a molecular orbital perspective. Ga(*s*)–Te(*p*) coupling forms a bonding manifold in the deep valence region and an antibonding counterpart that constitutes the conduction-band edge. The Cd–Te interaction, through *p*–*d* orbital hybridization, forms bonding states within

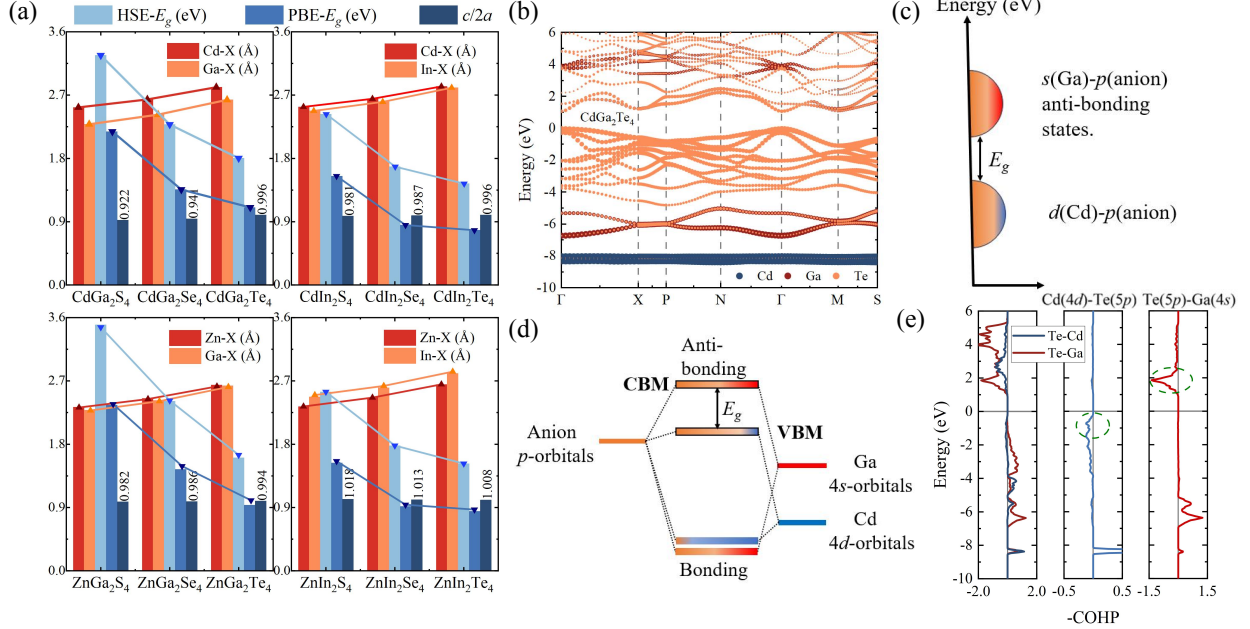


FIG. 3. (a) Calculation results of bond lengths, electronic band gaps (PBE/HSE), and structural parameter η for defective chalcopyrites. Line graphs visualize parameter trends. To visualize the variation of $\eta = |2 - c/a|$ in the figure, $c/2a$ is used here instead. (b) The atom-projected band structure of CdGa₂Te₄. Bubble sizes (all with a scaling factor of 15) represent the electronic state contributions from Te, Ga, and Cd. (c) Schematic DOS with Cd-anion antibonding as the valence band edge and Ga-anion antibonding states as the conduction band edge. (d) Schematic molecular-orbital diagram. The Cd 4*d* atomic orbitals and the anion *p*-states form antibonding states that are expected to reside near the valence band edge. The Ga 4*s* atomic orbitals and the anion *p*-states form antibonding states that are expected to appear at the conduction band edge. (e) Crystal Orbital Hamilton Population. The left represents the total interactions of Te–Cd and Te–Ga. The middle and right show the interactions for Cd-4*d*/Te-5*p* and Ga-4*s*/Te-5*p*, respectively. Green circles mark the energy positions of the corresponding antibonding states. Positive values correspond to bonding states, while negative values correspond to antibonding states.

the valence band and generates antibonding states near the Te 5*p*-dominated VBM, which exhibit weak Cd–Te antibonding characteristics. The Crystal Orbital Hamilton Population (COHP) [71] in FIG. 3(e) further supports the finding by revealing antibonding characters associated with Ga–Te near the CBM and Cd–Te near the VBM. The anion evolution trend further validates this mechanism. as the electronegativity of the VI-site anion decreases

with the cation fixed, the metal–anion bonds become longer and the hybridization weakens, which reduces the bonding–antibonding splitting; together with the upward shift of the anion- p energy level for heavier chalcogens, this drives the VBM upward and tends to lower the antibonding CBM, resulting in an overall narrowing of E_g .

The reduction in band gap E_g typically lowers the energy threshold for electrons to be excited from the VBM to the CBM, leading to an increase in intrinsic carrier concentration and ultimately enhancing the electrical conductivity σ as shown in FIG. S13. The microscopic origin of the variation in σ was further probed through a systematic analysis of the three dominant carrier-scattering mechanisms: ADP, IMP, and POP. These mechanisms directly determine σ by governing the carrier mobility μ ($\sigma = ne\mu$) [72]. The influence of scattering mechanisms on mobility follows a reciprocal relationship, i.e., carrier mobility is inversely proportional to the total scattering rate. Therefore, a low scattering rate of a scattering mechanism indicates weaker hindrance to carrier motion, which is conducive to achieving higher mobility. FIGs. 4(a) and (b) present the variations in mobility for mechanisms as functions of carrier concentration and scattering rates in CdGa₂Te₄ and ZnGa₂S₄, respectively. At 300 K and a carrier concentration of 10^{21} cm⁻³, the scattering rate of ADP in both CdGa₂Te₄ and ZnGa₂S₄ is one order of magnitude lower than that of POP and IMP. Moreover, the scattering rates for mechanisms in CdGa₂Te₄ are slightly lower than those in ZnGa₂S₄. A similar trend is observed for mobility—dominated by ADP in both materials—which drops sharply when the carrier concentration exceeds 10^{19} cm⁻³. Remarkably, the mobility of CdGa₂Te₄ is one order of magnitude higher than that of ZnGa₂S₄, indicating its significantly higher σ .

FIG. 4(c) presents the carrier concentration dependence of σ , Seebeck coefficient S , electronic thermal conductivity κ_e , and power factor PF for CdGa₂Te₄ and ZnGa₂S₄. As discussed earlier, CdGa₂Te₄ exhibits significantly higher σ than ZnGa₂S₄. And this disparity becomes even more pronounced with increasing carrier concentration. In contrast to the upward trend of σ , the S of both materials gradually decreases as carrier concentration increases. ZnGa₂S₄ maintains a slightly higher S than CdGa₂Te₄ overall, which is closely related to their differences in band structure. As shown in FIG. S10, ZnGa₂S₄ possesses higher band degeneracy near the VBM. Its hole effective masses along the Γ –N and Γ –M directions ($0.766 m_0$ and $0.578 m_0$) are substantially larger than the corresponding values for CdGa₂Te₄ ($0.61 m_0$ and $0.321 m_0$). Since the S is positively correlated with carrier ef-

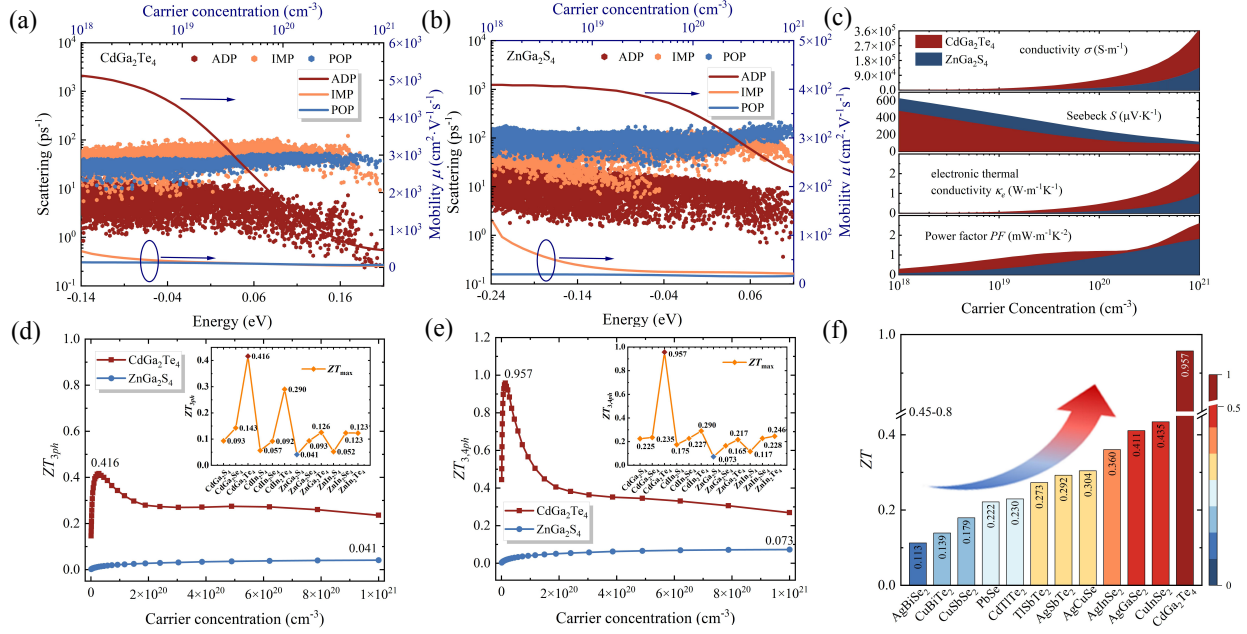


FIG. 4. The scattering rates of ADP, IMP, and POP mechanisms for (a) ZnGa_2S_4 and (b) CdGa_2Te_4 at 300 K and a carrier concentration of 10^{21} cm^{-3} . The carrier mobilities of ADP, IMP, and POP mechanisms for (a) ZnGa_2S_4 and (b) CdGa_2Te_4 as a function of carrier concentration. The scatter points represent the scattering rates, and the lines represent the mobilities. The colors red, orange, and blue represent ADP, IMP, and POP, respectively. (c) The calculated results of σ , S , κ_e , and PF of ZnGa_2S_4 and CdGa_2Te_4 with varying carrier concentrations. Blue represents ZnGa_2S_4 , and red represents CdGa_2Te_4 . (d) The variation of ZT_{3ph} of ZnGa_2S_4 and CdGa_2Te_4 with carrier concentration considering. The illustration shows the maximum ZT_{3ph} for defective chalcopyrites. (e) The variation of $ZT_{3,4ph}$ of ZnGa_2S_4 and CdGa_2Te_4 with carrier concentration. The illustration shows the maximum $ZT_{3,4ph}$ for defective chalcopyrites. (f) Comparison of ZT between CdGa_2Te_4 and other typical thermoelectric compounds at 300 K, where the specific compounds corresponding to the labels are detailed in the ref. [73–78].

fective mass, ZnGa_2S_4 consequently exhibits relatively higher S values. Based on the above electronic transport parameters, we further calculated the evolution of the PF with carrier concentration. Despite the coupling relationship between S and σ , CdGa_2Te_4 ultimately achieves an excellent PF owing to its considerably higher σ . Additionally, the carrier concentration dependence of κ_e follows essentially the same trend as σ , which is expected due to the Wiedemann–Franz law ($\kappa_e = L\sigma T$, where L is the Lorenz number) [79]. It is worth

emphasizing that when evaluating the total thermal conductivity of these materials, the contribution from κ_e cannot be neglected. The κ_e is comparable to or even higher than that of κ_L at elevated carrier concentrations.

FIGs. 4(d) and (e) present the evolution of ZT with carrier concentration for CdGa_2Te_4 and ZnGa_2S_4 at 300 K to evaluate the influence of $4ph$ scattering by comparing the results under two scenarios: one considering only $3ph$ scattering (ZT_{3ph}) and another incorporating both $3ph$ and $4ph$ scattering ($ZT_{3,4ph}$). Benefiting from an ultralow κ_L and a high PF , CdGa_2Te_4 exhibits excellent thermoelectric potential at 300 K. Its ZT_{3ph} already reaches 0.416, being ten times larger than that of ZnGa_2S_4 (0.041). The inclusion of $4ph$ scattering enhances ZT for both materials, although the magnitude of the enhancement differs. CdGa_2Te_4 shows a dramatic rise in value from 0.416 to 0.957, corresponding to a ~ 2.4 times increase, whereas ZnGa_2S_4 exhibits only a modest increase from 0.041 to 0.073, marking a ~ 1.8 times enhancement. This reveals that $4ph$ scattering plays a decisive role in defective chalcopyrites. In addition, the ZT increases monotonically as the electronegativity of the VI-site anion decreases with the cation fixed. Such a trend aligns with the enhancement in σ shown in FIG. S13. A comparative summary of the carrier concentration-dependent ZT_{3ph} and $ZT_{3,4ph}$ for the defective chalcopyrites is provided in Supplementary FIG. S14.

Finally, we compared the ZT of CdGa_2Te_4 with those of several representative thermoelectric materials at 300 K. As illustrated in FIG. 4(f), CdGa_2Te_4 achieves an outstanding ZT of 0.957. This value drastically outperforms the other candidate materials evaluated—such as traditional PbSe [77] and chalcopyrites (e.g., AgSbTe_2 [76] and TlSbTe_2 [78])—whose ZT values generally fall below 0.45. The significant performance improvement demonstrates that defective chalcopyrites with intrinsic vacancies, particularly CdGa_2Te_4 , exhibit immense potential as high-performance thermoelectric materials. This excellent performance is mainly attributed to the strong lattice anharmonicity caused by its unique ordered intrinsic vacancy structure. Such anharmonicity significantly enhances $4ph$ scattering and reduces κ_L to an ultra-low level. Meanwhile, the band structure ensures excellent electrical transport properties, enabling a favorable balance between thermal and electrical performance. Our findings not only reveal the critical role of vacancies in regulating thermal transport properties but also provide a new strategy for exploring next-generation high-performance thermoelectric materials.

IV. CONCLUSION

In summary, we have systematically elucidated the structure-property relationship governing thermoelectric performance in defective chalcopyrites. Ordered intrinsic vacancies are identified as the central structural motif responsible for their exceptional thermal transport behavior. By further lowering crystal symmetry and amplifying local lattice distortion, vacancy ordering induces pronounced lattice anharmonicity, promotes metavalent-bonding character, and strengthens higher-order phonon interactions. Together with soft low-frequency phonons, strongly negative Grüneisen parameters, and reduced phonon group velocities, these effects make four-phonon scattering a dominant heat-resistance mechanism and drive the lattice thermal conductivity to ultralow values. At the same time, the VI-site anion serves as an effective electronic tuning knob: decreasing anion electronegativity elongates metal-anion bonds, weakens orbital hybridization, shifts anion p states upward, and narrows the band gap, thereby enhancing carrier transport. Owing to this synergistic optimization of phonon and electronic properties, CdGa_2Te_4 exhibits the best overall thermoelectric performance, with a lattice thermal conductivity of $0.19 \text{ W}\cdot\text{m}^{-1}\text{K}^{-1}$ and a room-temperature ZT of 0.957. Beyond identifying a high-performing compound, this work establishes vacancy ordering and anion engineering as a unified design principle for developing next-generation thermoelectric materials based on defective chalcopyrite frameworks.

V. ACKNOWLEDGEMENT

H. Zhang and J.C. Yue contributed equally to this work. H. Zhang and Y.H. Liu acknowledge the National Key Research and Development Program of China (No. 2023YFA1406200) and the Institute of High-pressure Physics of Ningbo University for its computational resources. J.C. Yue acknowledges the China Scholarship Council (No. 202408330112). H. Gao and Y.-W. Fang acknowledge the financial support received from the IKUR Strategy under the collaboration agreement between Ikerbasque Foundation and Centro de Física de Materiales (CFM-MPC) on behalf of the Department of Science, Universities and Innovation of the Basque Government (HPCAI21: AI-CrysPred). Y.-W. Fang is partially supported by the Extraordinary Grant of CSIC (No. 2025ICT122). W.L. Ren acknowledges the NHR-Verein e.V.(www.nhr-verein.de) for supporting this work within the NHR Graduate School

of National High Performance Computing (NHR). S.Y. Lin acknowledges the computation resources provided by the National Academic Infrastructure for Supercomputing in Sweden (NAISS) – at supercomputer centers NSC and PDC, partially funded by the Swedish Research Council through grant agreement No. 2022-06725 – and by the Vienna Scientific Cluster (VSC) in Austria.

- [1] Hongyao Xie, Shiqiang Hao, Trevor P Bailey, Songting Cai, Yinying Zhang, Tyler J Slade, G Jeffrey Snyder, Vinayak P Dravid, Ctirad Uher, Christopher Wolverton, et al. Ultralow thermal conductivity in diamondoid structures and high thermoelectric performance in $(\text{Cu}_{1-x}\text{Ag}_x)(\text{In}_{1-y}\text{Ga}_y)\text{Te}_2$. *Journal of the American Chemical Society*, 143(15):5978–5989, 2021.
- [2] Ruoxi Li, Xin Li, Lili Xi, Jiong Yang, David J Singh, and Wenqing Zhang. High-throughput screening for advanced thermoelectric materials: diamond-like ABX_2 compounds. *ACS Applied Materials & Interfaces*, 11(28):24859–24866, 2019.
- [3] Lei Hu, Yubo Luo, Yue-Wen Fang, Feiyu Qin, Xun Cao, Hongyao Xie, Jiawei Liu, Jinfeng Dong, Andrea Sanson, Marco Giarola, et al. High thermoelectric performance through crystal symmetry enhancement in triply doped diamondoid compound Cu_2SnSe_3 . *Advanced Energy Materials*, 11(42):2100661, 2021.
- [4] Hongyao Xie, Li-Dong Zhao, and Mercouri G Kanatzidis. Lattice dynamics and thermoelectric properties of diamondoid materials. *Interdisciplinary Materials*, 3(1):5–28, 2024.
- [5] Kyunghan Ahn, Hocheol Shin, Jino Im, Sang Hyun Park, and In Chung. ZnTe alloying effect on enhanced thermoelectric properties of p -type PbTe. *ACS Applied Materials & Interfaces*, 9(4):3766–3773, 2017.
- [6] Yu Xiao and Li-Dong Zhao. Charge and phonon transport in PbTe-based thermoelectric materials. *Npj Quantum Materials*, 3(1):55, 2018.
- [7] Takuya Tanimoto, Koichiro Suekuni, Taiki Tanishita, Hidetomo Usui, Terumasa Tadano, Taiga Kamei, Hikaru Saito, Hirotaka Nishiata, Chul Ho Lee, Kazuhiko Kuroki, et al. Enargite Cu_3PS_4 : A Cu-S-Based thermoelectric material with a wurtzite-derivative structure. *Advanced Functional Materials*, 30(22):2000973, 2020.

- [8] Hong Pang, Cedric Bourges, Rajveer Jha, Takahiro Baba, Naoki Sato, Naoyuki Kawamoto, Tetsuya Baba, Naohito Tsujii, and Takao Mori. Revealing an elusive metastable wurtzite CuFeS_2 and the phase switching between wurtzite and chalcopyrite for thermoelectric thin films. *Acta Materialia*, 235:118090, 2022.
- [9] Jian Zhang, Lulu Huang, Chen Zhu, Chongjian Zhou, Bushra Jabar, Jimin Li, Xiaoguang Zhu, Ling Wang, Chunjun Song, Hongxing Xin, et al. Design of domain structure and realization of ultralow thermal conductivity for record-high thermoelectric performance in chalcopyrite. *Advanced Materials*, 31(52):1905210, 2019.
- [10] Yu Cao, Xianli Su, Fanchen Meng, Trevor P Bailey, Jinggeng Zhao, Hongyao Xie, Jian He, Ctirad Uher, and Xinfeng Tang. Origin of the distinct thermoelectric transport properties of chalcopyrite ABTe_2 ($A = \text{Cu, Ag}$; $B = \text{Ga, In}$). *Advanced Functional Materials*, 30(51):2005861, 2020.
- [11] Ami Nomura, Seongho Choi, Manabu Ishimaru, Atsuko Kosuga, Thomas Chasapis, Saneyuki Ohno, G Jeffrey Snyder, Yuji Ohishi, Hiroaki Muta, Shinsuke Yamanaka, et al. Chalcopyrite ZnSnSb_2 : a promising thermoelectric material. *ACS Applied Materials & Interfaces*, 10(50):43682–43690, 2018.
- [12] Siqi Guo, Jincheng Yue, Jiongzhi Zheng, Hui Zhang, Ning Wang, Junda Li, Yanhui Liu, and Tian Cui. Bidirectional optimization of transport properties for thermoelectric performance via hydrostatic pressure in chalcopyrite AgXTe_2 ($X = \text{In, Ga}$). *Physical Review B*, 111(18):184312, 2025.
- [13] Yongheng Li, Junyan Liu, and Jiawang Hong. Anharmonicity-induced strong temperature-dependent thermal conductivity in CuInX_2 ($X = \text{Se, Te}$). *Physical Review B*, 106(9):094317, 2022.
- [14] Jincheng Yue, Siqi Guo, Junda Li, Jiahui Zhao, Chen Shen, Hongbin Zhang, Yanhui Liu, and Tian Cui. Pressure-induced remarkable four-phonon interaction and enhanced thermoelectric conversion efficiency in CuInTe_2 . *Materials Today Physics*, 39:101283, 2023.
- [15] Anna Miglio, Christophe P Heinrich, Wolfgang Tremel, Geoffroy Hautier, and Wolfgang G Zeier. Local bonding influence on the band edge and band gap formation in quaternary chalcopyrites. *Advanced Science*, 4(9):1700080, 2017.
- [16] Jiaman Wei, Wei Yu, Zhijian Li, Jiaxin Hu, Tonghui Wang, Yuan Yu, and Xin Guo. Pressure-mediated band engineering and cation ordering for enhanced thermoelectric performance in

- CuInTe₂ chalcopyrites. *Chemical Engineering Journal*, page 166531, 2025.
- [17] Sitong Luo, Yujin Wang, Jingxuan Liang, Yuntian Jiang, Zhibo Wei, Yifan Du, Liang Lv, Shuqi Zheng, and Weiyu Song. Realizing high thermoelectric performance of CuGaTe₂ via CdTe-doping-driven band engineering and chemical bond modulation. *Journal of Materiomics*, page 101089, 2025.
- [18] Xiaojian Tan, Ling Wang, Hezhu Shao, Song Yue, Jingtao Xu, Guoqiang Liu, Haochuan Jiang, and Jun Jiang. Improving thermoelectric performance of α -MgAgSb by theoretical band engineering design. *Advanced Energy Materials*, 7(18):1700076, 2017.
- [19] Ning Wang, Jincheng Yue, Hui Zhang, Siqi Guo, Shuli Li, Yuanhong Tao, Yanhui Liu, and Tian Cui. Achieving decoupled thermal and electrical transport in BaLiX (X= P, As, Sb, Bi) Zintl phase compounds via anion engineering. *Materials Today Physics*, page 101974, 2025.
- [20] Hongyao Xie, Yukun Liu, Yinying Zhang, Shiqiang Hao, Zhi Li, Matthew Cheng, Songting Cai, G Jeffrey Snyder, Christopher Wolverton, Ctirad Uher, et al. High thermoelectric performance in chalcopyrite Cu_{1-x}Ag_xGaTe₂-ZnTe: Nontrivial band structure and dynamic doping effect. *Journal of the American Chemical Society*, 144(20):9113–9125, 2022.
- [21] Dipanshu Bansal. Aliovalence-doped thermoelectrics. *Joule*, 7(10):2203–2205, 2023.
- [22] Suniya Siddique, Ghulam Abbas, Manzar Mushaf Yaqoob, Jian Zhao, RuiHua Chen, J Andreas Larsson, Yuede Cao, Yuexing Chen, Zhuanghao Zheng, Dongping Zhang, et al. Optimization of thermoelectric performance in *p*-type SnSe crystals through localized lattice distortions and band convergence. *Advanced Science*, 12(7):2411594, 2025.
- [23] Hui Pan, Lixia Zhang, Huiyuan Geng, Qing Chang, Bo Zhang, and Zhan Sun. Lattice distortion realizing the treble-high thermoelectric module. *Materials Today Physics*, 50:101635, 2025.
- [24] Qi Zhang, Bingchuan Gu, Yehao Wu, Tiejun Zhu, Teng Fang, Yuxi Yang, Jiandang Liu, Bangjiao Ye, and Xinbing Zhao. Evolution of the intrinsic point defects in bismuth telluride-based thermoelectric materials. *ACS Applied Materials & Interfaces*, 11(44):41424–41431, 2019.
- [25] Hongyao Xie, Emil S Bozin, Zhi Li, Milinda Abeykoon, Soham Banerjee, James P Male, G Jeffrey Snyder, Christopher Wolverton, Simon JL Billinge, and Mercouri G Kanatzidis. Hidden local symmetry breaking in silver diamondoid compounds is root cause of ultralow thermal conductivity. *Advanced Materials*, 34(24):2202255, 2022.

- [26] Tawat Suriwong, Ken Kurosaki, Somchai Thongtem, Adul Harnwunggmoung, Theerayuth Plirdpring, Tohru Sugahara, Yuji Ohishi, Hiroaki Muta, and Shinsuke Yamanaka. Synthesis and thermal conductivities of ZnIn_2Te_4 and CdIn_2Te_4 with defect-chalcopyrite structure. *Journal of alloys and compounds*, 509(27):7484–7487, 2011.
- [27] Prakash Govindaraj, Mugundhan Sivasamy, Kowsalya Murugan, Kathirvel Venugopal, and Pandiyarasan Veluswamy. Pressure-driven thermoelectric properties of defect chalcopyrite structured ZnGa_2Te_4 : Ab initio study. *RSC Advances*, 12(20):12573–12582, 2022.
- [28] Fang Yu, Xiang Meng, Jiang Cheng, Jianping Liu, Yali Yao, and Jie Li. Novel n -type thermoelectric material of ZnIn_2Se_4 . *Journal of Alloys and Compounds*, 797:940–944, 2019.
- [29] Prakash Govindaraj, Kowsalya Murugan, Pandiyarasan Veluswamy, and Kathirvel Venugopal. Ordered-vacancy defect chalcopyrite ZnIn_2Te_4 : A potential thermoelectric material with low lattice thermal conductivity. *Journal of Solid State Chemistry*, 324:124076, 2023.
- [30] G. Kresse and J. Furthmüller. Efficiency of ab-initio total energy calculations for metals and semiconductors using a plane-wave basis set. *Computational Materials Science*, 6:15–50, 1996.
- [31] Georg Kresse and Jürgen Furthmüller. Efficient iterative schemes for ab initio total-energy calculations using a plane-wave basis set. *Physical Review B*, 54(16):11169, 1996.
- [32] John P Perdew, Adrienn Ruzsinszky, Gábor I Csonka, Oleg A Vydrov, Gustavo E Scuseria, Lucian A Constantin, Xiaolan Zhou, and Kieron Burke. Restoring the density-gradient expansion for exchange in solids and surfaces. *Physical Review letters*, 100(13):136406, 2008.
- [33] Angel Albavera-Mata, Karla Botello-Mancilla, SB Trickey, José L Gázquez, and Alberto Vela. Generalized gradient approximations with local parameters. *Physical Review B*, 102(3):035129, 2020.
- [34] Peter E Blöchl. Projector augmented-wave method. *Physical Review B*, 50(24):17953, 1994.
- [35] Alexander V Shapeev. Moment tensor potentials: A class of systematically improvable interatomic potentials. *Multiscale Modeling & Simulation*, 14(3):1153–1173, 2016.
- [36] Ivan S Novikov, Konstantin Gubaev, Evgeny V Podryabinkin, and Alexander V Shapeev. The mlip package: moment tensor potentials with mpi and active learning. *Machine Learning: Science and Technology*, 2(2):025002, 2020.
- [37] Ruihao Tan, Kaiwang Zhang, and Yue-Wen Fang. Ultralow thermal conductivity via weak interactions in PbSe/PbTe monolayer heterostructure for thermoelectric design. *Journal of Materials Informatics*, 5(4), 2025.

- [38] Guiyan Dong, Tian Cui, Zihao Huo, Zhengtao Liu, Wenxuan Chen, Pugeng Hou, Yue-Wen Fang, and Defang Duan. Machine-learning potentials for quantum and anharmonic effects in superconducting $Fm\bar{3}m$ LaBeH₈. *Materials Today Physics*, 59:101939, 2025.
- [39] Han Wang, Linfeng Zhang, Jiequn Han, et al. Deepmd-kit: A deep learning package for many-body potential energy representation and molecular dynamics. *Computer Physics Communications*, 228:178–184, 2018.
- [40] Linfeng Zhang, Jiequn Han, Han Wang, Roberto Car, and Weinan E. Deep potential molecular dynamics: a scalable model with the accuracy of quantum mechanics. *Physical Review letters*, 120(14):143001, 2018.
- [41] Florian Knoop, Thomas Purcell, Matthias Scheffler, and Christian Carbogno. Fhi-vibes: Ab initio vibrational simulations. *The Journal of Open Source Software*, 5(56), 2020.
- [42] Keivan Esfarjani and Harold T Stokes. Method to extract anharmonic force constants from first principles calculations. *Physical Review B—Condensed Matter and Materials Physics*, 77(14):144112, 2008.
- [43] Atsushi Togo and Isao Tanaka. First principles phonon calculations in materials science. *Scripta Materialia*, 108:1–5, 2015.
- [44] Atsushi Togo. First-principles phonon calculations with phonopy and phono3py. *Journal of the Physical Society of Japan*, 92(1):012001, 2023.
- [45] Wu Li, Jesús Carrete, Nebil A Katcho, and Natalio Mingo. Shengbte: A solver of the boltzmann transport equation for phonons. *Computer Physics Communications*, 185(6):1747–1758, 2014.
- [46] Zherui Han, Xiaolong Yang, Wu Li, Tianli Feng, and Xiulin Ruan. Fourphonon: An extension module to shengbte for computing four-phonon scattering rates and thermal conductivity. *Computer Physics Communications*, 270:108179, 2022.
- [47] Michele Simoncelli, Nicola Marzari, and Francesco Mauri. Unified theory of thermal transport in crystals and glasses. *Nature Physics*, 15(8):809–813, 2019.
- [48] Jincheng Yue, Yanhui Liu, and Jiongzhi Zheng. Interlayer thermal transport and glasslike behavior in crystalline CsCu₄Se₃. *Physical Review B*, 111(2):024313, 2025.
- [49] Jochen Heyd, Gustavo E Scuseria, and Matthias Ernzerhof. Hybrid functionals based on a screened coulomb potential. *The Journal of Chemical Physics*, 118(18):8207–8215, 2003.

- [50] Alex M Ganose, Junsoo Park, Alireza Faghaninia, Rachel Woods-Robinson, Kristin A Persson, and Anubhav Jain. Efficient calculation of carrier scattering rates from first principles. *Nature Communications*, 12(1):2222, 2021.
- [51] Dat D Vo, Tuan V Vu, AI Kartamyshev, Thi H Ho, and Kieu-My Bui. Enhancing InSe monolayer via full hydrogenation: insights into electronic structure, piezoelectricity, and charge mobility. *RSC Advances*, 15(30):24236–24246, 2025.
- [52] DL Rode. Low-field electron transport. In *Semiconductors and Semimetals*, volume 10, pages 1–89. Elsevier, 1975.
- [53] Yandong Sun, Yanguang Zhou, Jian Han, Wei Liu, Cewen Nan, Yuanhua Lin, Ming Hu, and Ben Xu. Strong phonon localization in PbTe with dislocations and large deviation to matthiessen’s rule. *Npj Computational Materials*, 5(1):97, 2019.
- [54] Félix Mouhat and François-Xavier Coudert. Necessary and sufficient elastic stability conditions in various crystal systems. *Physical Review B*, 90(22):224104, 2014.
- [55] James E Saal, Scott Kirklin, Muratahan Aykol, Bryce Meredig, and Christopher Wolverton. Materials design and discovery with high-throughput density functional theory: the open quantum materials database (OQMD). *Jom*, 65(11):1501–1509, 2013.
- [56] Scott Kirklin, James E Saal, Bryce Meredig, Alex Thompson, Jeff W Doak, Muratahan Aykol, Stephan Rühl, and Chris Wolverton. The open quantum materials database (OQMD): assessing the accuracy of DFT formation energies. *Npj Computational Materials*, 1(1):1–15, 2015.
- [57] Won-Seon Seo, Riki Otsuka, Harumi Okuno, Mitsuru Ohta, and Kunihiro Koumoto. Thermoelectric properties of sintered polycrystalline ZnIn_2S_4 . *Journal of Materials Research*, 14(11):4176–4181, 1999.
- [58] Florian Knoop, Thomas AR Purcell, Matthias Scheffler, and Christian Carbogno. Anharmonicity in thermal insulators: An analysis from first principles. *Physical Review Letters*, 130(23):236301, 2023.
- [59] Jean-Yves Raty, Mathias Schumacher, Pavlo Golub, Volker L Deringer, Carlo Gatti, and Matthias Wuttig. A quantum-mechanical map for bonding and properties in solids. *Advanced Materials*, 31(3):1806280, 2019.
- [60] Chenyang Wang, Quanying Ma, Huarui Xue, Qin Wang, Pengfei Luo, Jiong Yang, Wenqing Zhang, and Jun Luo. Tetrahedral distortion and thermoelectric performance of the ag-substituted CuInTe_2 chalcopyrite compound. *ACS Applied Energy Materials*, 3(11):11015–

- 11023, 2020.
- [61] Hao Yu, Liu-Cheng Chen, Hong-Jie Pang, Peng-Fei Qiu, Qing Peng, and Xiao-Jia Chen. Temperature-dependent phonon anharmonicity and thermal transport in CuInTe₂. *Physical Review B*, 105(24):245204, 2022.
- [62] Florian Knoop, Thomas AR Purcell, Matthias Scheffler, and Christian Carbogno. Anharmonicity measure for materials. *Physical Review Materials*, 4(8):083809, 2020.
- [63] BRIAN W Petley. The atomic mass unit. *IEEE Transactions on Instrumentation and Measurement*, 38(2):175–179, 2002.
- [64] Yuan Yu, Matteo Cagnoni, Oana Cojocaru-Mirédin, and Matthias Wuttig. Chalcogenide thermoelectrics empowered by an unconventional bonding mechanism. *Advanced Functional Materials*, 30(8):1904862, 2020.
- [65] Loay Elalfy, Denis Music, and Ming Hu. Metavalent bonding induced abnormal phonon transport in diamondlike structures: Beyond conventional theory. *Physical Review B*, 103(7):075203, 2021.
- [66] Jincheng Yue, Yanhui Liu, Wenling Ren, Shuyao Lin, Chen Shen, Harish Kumar Singh, Tian Cui, Terumasa Tadano, and Hongbin Zhang. Role of atypical temperature-responsive lattice thermal transport on the thermoelectric properties of antiperovskites Mg₃XN (X= P, As, Sb, Bi). *Materials Today Physics*, 41:101340, 2024.
- [67] Kunpeng Yuan, Xiaoliang Zhang, Yufei Gao, and Dawei Tang. Soft phonon modes lead to suppressed thermal conductivity in Ag-based chalcopyrites under high pressure. *Physical Chemistry Chemical Physics*, 25(36):24883–24893, 2023.
- [68] Jincheng Yue, Jiongzhi Zheng, Junda Li, Siqi Guo, Wenling Ren, Han Liu, Yanhui Liu, and Tian Cui. Ultralow glassy thermal conductivity and controllable, promising thermoelectric properties in crystalline o-CsCu₅S₃. *ACS Applied Materials & Interfaces*, 16(16):20597–20609, 2024.
- [69] Jincheng Yue, Jiongzhi Zheng, Xingchen Shen, Krishnendu Maji, Chun-Chuen Yang, Shuyao Lin, Pierric Lemoine, Emmanuel Guilmeau, Yanhui Liu, and Tian Cui. Diffuson-dominated thermal transport crossover from ordered to liquid-like Cu₃BiS₃: The negligible role of ion hopping. *Small*, 21(42):e06386, 2025.
- [70] Peter Atkins. *Shriver and Atkins' inorganic chemistry*. Oxford University Press, USA, 2010.

- [71] Richard Dronskowski and Peter E Bloechl. Crystal orbital hamilton populations (COHP): energy-resolved visualization of chemical bonding in solids based on density-functional calculations. *The Journal of Physical Chemistry*, 97(33):8617–8624, 1993.
- [72] Neil W Ashcroft and N David Mermin. Solid state physics. *Google Scholar*, 403, 2005.
- [73] Zhi-Gang Chen, Xiaolei Shi, Li-Dong Zhao, and Jin Zou. High-performance SnSe thermoelectric materials: Progress and future challenge. *Progress in Materials Science*, 97:283–346, 2018.
- [74] Jiasheng Liang, Tuo Wang, Pengfei Qiu, Shiqi Yang, Chen Ming, Hongyi Chen, Qingfeng Song, Kunpeng Zhao, Tian-Ran Wei, Dudi Ren, et al. Flexible thermoelectrics: from silver chalcogenides to full-inorganic devices. *Energy & Environmental Science*, 12(10):2983–2990, 2019.
- [75] Zipei Zhang, Wenhao Li, Lu Yu, Sitong Wei, Shikai Wei, Zhen Ji, Weiyu Song, and Shuqi Zheng. Defect engineering synergistically modulates power factor and thermal conductivity of CuGaTe₂ for ultra-high thermoelectric performance. *Journal of Materials Science & Technology*, 128:213–220, 2022.
- [76] Nan-Hai Li, Qiang Zhang, Xiao-Lei Shi, Jun Jiang, and Zhi-Gang Chen. Silver copper chalcogenide thermoelectrics: advance, controversy, and perspective. *Advanced Materials*, 36(37):2313146, 2024.
- [77] Shibo Liu, Yongxin Qin, Yi Wen, Haonan Shi, Bingchao Qin, Tao Hong, Xiang Gao, Qian Cao, Cheng Chang, and Li-Dong Zhao. Efforts toward the fabrication of thermoelectric cooling module based on *n*-type and *p*-type PbTe ingots. *Advanced Functional Materials*, 34(26):2315707, 2024.
- [78] Heng Wang, Anek Charoenphakdee, Ken Kurosaki, Shinsuke Yamanaka, and G Jeffrey Snyder. Reduction of thermal conductivity in pbte: Tl by alloying with TlSbTe₂. *Physical Review B—Condensed Matter and Materials Physics*, 83(2):024303, 2011.
- [79] GV Chester and A Thellung. The law of wiedemann and franz. *Proceedings of the Physical Society*, 77(5):1005–1013, 1961.